PONTIFICIA UNIVERSIDAD CATÓLICA DE CHILE
ESCUELA DE INGENIERÍA

AN AUTOCORRELATION-BASED BAYESIAN ESTIMATOR FOR ACOUSTIC-RADIATION-FORCE-INDUCED DISPLACEMENTS.

STEFAN WERNER KLEMMER CHANDÍA

Thesis submitted to the Office of Research and Graduate Studies
in partial fulfillment of the requirements for the degree of
Master of Science in Engineering

Advisor:
PATRICIO DE LA CUADRA BANDERAS
JOAQUÍN MURA MARDONES

Santiago de Chile, March 2023

PONTIFICIA UNIVERSIDAD CATÓLICA DE CHILE
ESCUELA DE INGENIERÍA

AN AUTOCORRELATION-BASED BAYESIAN ESTIMATOR FOR ACOUSTIC-RADIATION-FORCE-INDUCED DISPLACEMENTS.

STEFAN WERNER KLEMMER CHANDÍA

Members of the Committee:
PATRICIO DE LA CUADRA BANDERAS
JOAQUÍN MURA MARDONES
CLAUDIA PRIETO VASQUEZ
JULIO SOTELO PARRAGUEZ
CÉSAR SÁEZ NAVARRETE

Thesis submitted to the Office of Research and Graduate Studies
in partial fulfillment of the requirements for the degree of
Master of Science in Engineering

Santiago de Chile, March 2023

Gratefully to my friends and family

ACKNOWLEDGEMENTS

First, I'd like to thank Dr. Juan Pablo Arab and Dr. Luis Antonio Díaz for guiding my initial steps in this research.

Second, I'm also thankful of prof. Joaquín Mura, who helped me test my methods on a hardware ultrasound device and gave me advise on my path towards becoming a researcher.

Third, I'd like to thank my research team, Fernando Hurtado, Joaquín Sepúlveda, Andrés González and prof. Patricio de la Cuadra, for listening to my presentations and sharing their own extraordinary investigations with me.

Last but not least, this thesis was supported by the following funds granted by the *Agencia Nacional de Investigación y Desarrollo* (ANID):

- FONDECYT 1201551.
- FONDEQUIP EQM210141: "Equipamiento para Laboratorio de Ultrasonido Cuantitativo de Investigación Interdisciplinar y Multipropósito Avanzado".

TABLE OF CONTENTS

LIST OF FIGURES

LIST OF TABLES

ABSTRACT

Displacement estimation algorithms play a critical role in the performance of ultrasound elastography methods. Bayesian displacement estimators have shown promising results in the last decade. However, computational cost still prevents their real-time implementation. In this thesis, a novel likelihood function called "autocorrelation kernel" (ACK) is incorporated into a bayesian estimator. Unlike previous approaches, ACK can directly evaluate the probability of sub-sample displacements without the need of oversampling or interpolation.

Representative B-mode images of shear wave elasticity imaging (SWEI) were generated. First, acoustic radiation force distributions were virtually simulated. Second, the finite element method was used to simulate realistic shear wave displacements. Finally, an ultrasound imaging software was used to produce images of moving tissue with appropriate speckle texture.

The proposed likelihood function was compared to the classical normalized cross-correlation function (NCC). Both functions were combined with a L1-norm prior to calculate the posterior distribution. Additionally, a L2-norm prior was tested with ACK. Displacement was estimated from the simulated B-mode images and results were compared in terms of bias, variance and root mean square error (RMSE).

NCC performed better than ACK by improving the initial, non-bayesian estimation between 24.2% and 42.5% in terms of RMSE. ACK made an improvement between 16.6% and 36.7% using L1-norm and 19.3% to 33.8% using L2-norm. Regarding computation time, ACK function evaluation was in average 28.6% faster than NCC. However, convergence of the non-linear optimization algorithm wasn't faster.

Keywords: elastography, ultrasound, displacement, estimation, bayesian.

RESUMEN

Los algoritmos de estimación de desplazamiento juegan un rol crítico en los métodos de elastografía por ultrasonido. Los estimadores bayesianos han mostrado resultados prometedores en la última década, pero su costo computacional impide su implementación en tiempo real. En esta tésis, una nueva función de verosimilitud llamada "*autocorrelation kernel*" (ACK) es incorporada a la estimación bayesiana. Al contrario de funciones anteriores, ACK permite evaluar directamente la probabilidad de desplazamientos sub-muestra sin necesitar sobremuestreo ni interpolación.

Se generaron imágenes de modo B representativas de *shear wave elasticity imaging* (SWEI). Primero, la fuerza de radiación acústica fue simulada. Segundo, el método de elementos finitos fue utilizado para simular desplazamientos de ondas cortantes. Por último, un programa de simulación de ultrasonido fue utilizado para producir imágenes de tejido en movimiento con textura apropiada.

La función de verosimilitud propuesta fue comparada contra la clásica correlación cruzada normalizada (NCC). Ambas fueron combinadas con un *prior* de norma L1 para calcular la probabilidad *a posteriori*. Adicionalmente, un *prior* de norma L2 fue probado con ACK. El desplazamiento fue estimado a partir de las imágenes de modo B simuladas y los resultados fueron comparados en términos de su sesgo, variabilidad y la raíz del error cuadrático medio (RMSE).

NCC tuvo un mejor desempeño que ACK. Esta mejoró la estimación inicial no bayesiana entre 24.2% y 42.5% en términos de su RMSE. ACK mejoró esta estimación en tan solo 16.6% a 36.7% con norma L1 y entre 19.3% y 33.8% con norma L2. Respecto al tiempo de cómputo, cada evaluación de ACK fue en promedio 28.6% más rápida que las de NCC. No obstante, la convergencia del algoritmo de optimización no-lineal no fue acelerada.

Palabras Claves: elastografía, ultrasonido, estimación, desplazamiento, bayesiana.

1. INTRODUCTION

Medical ultrasound (US) is an imaging technique that uses a transducer to generate images of human tissue. A transducer is equipped with an array of piezoelectric elements that transform electric signals into mechanical vibrations and vice-versa (Martin & Ramnarine, 2010). Figure 1.1 shows a linear array transducer with a common definition of the problem's spatial dimensions: lateral (x), elevational (y) and axial distance (z). The elements are excited with a short, bandpass electric pulse of central frequency f_c. Sound waves travel in the axial direction and whenever a wavefront encounters a small acoustic inhomogeneity (called "scatterer"), the pulse is partially reflected in the form of an "echo". Finally, the transducer transforms the received echo into an electric signal, which is sampled and processed to create an image. Thus, this is called "pulse-echo" imaging.

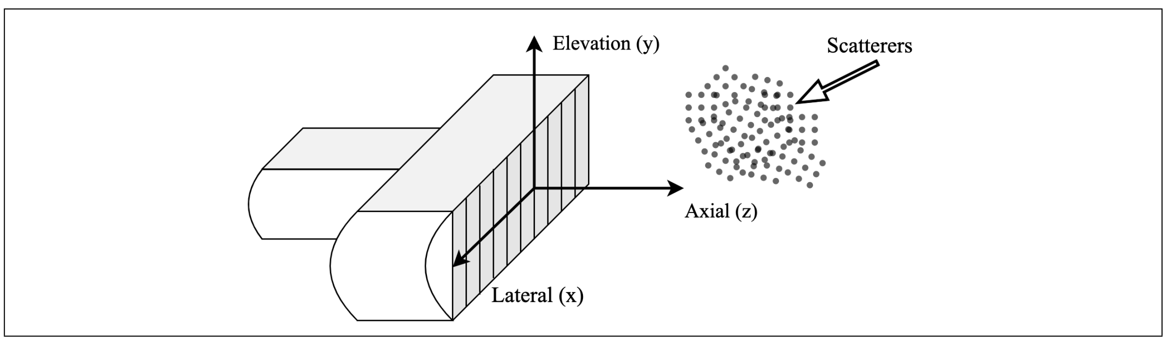

Figure 1.1. Linear array transducer and respective spatial dimensions.

Figure 1.2a depicts a received echo as a function of time t. As described by equation 1.1, time can be mapped to a spatial dimension z by considering that the speed of sound in human tissue c_s is approximately 1540 m/s (Martin & Ramnarine, 2010). Indeed, it is possible to infer the distance between transducer and scattering source. As shown in figure 1.2b, the spatial profile of the acoustic pressure will exhibit a wavelength of $\lambda = c_s/f_c$.

$$z = t\, c_s/2 \tag{1.1}$$

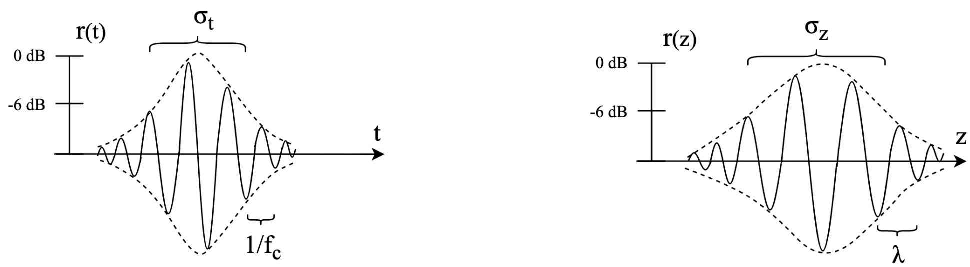

(a) Over time t.

(b) Over axial distance z.

Figure 1.2. Example of a received echo as a function of (a) time and (b) axial distance. σ_t and σ_z are full width half maximums (FWHM), i.e. the lengths of the segments where the amplitude of the envelope is greater than -6dB below its peak.

If many elements are distributed along the lateral dimension, it is also possible to infer the lateral position x of that source by using "beamforming", i.e. the combination of delayed versions of various element signals. This results in a bandpass, two-dimensional image, like figure 1.3a. The two-dimensional envelope of the beamformed signals is known as a "B-mode" image (see figure 1.3b). When imaging a dynamic phenomenon, many consecutive pulse-echo events can be used create a video-like collection of "frames". Digitally, all acquisitions are represented by a 3D matrix with dimensions of position and time: $r(x, z, T)$.

On the one hand, the spatial resolution of B-mode images depends on the transducer's geometry, number of elements and the pulse's envelope. It's limited by the "resolution cell" of the system, which corresponds to the ellipsoidal volume where the intensity of the response caused by a single scatterer is greater than -6 dB below its peak. It can be calculated using equation 1.2:

$$V_{\text{res. cell}} = \frac{\pi}{4}\,\sigma_x\,\sigma_y\,\sigma_z \tag{1.2}$$

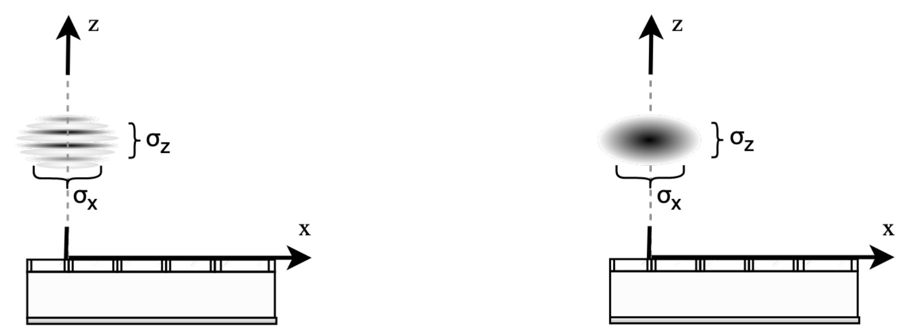

(a) Amplitude. (b) Envelope.

Figure 1.3. Pulse-echo acquisition in two dimensions, including (a) the signal's amplitude and (b) its envelope. The echo is produced by a single scaterer in front of the transducer.

where σ_x, σ_y and σ_z are the FWHM lengths of the response in every dimension, as shown in figure 1.3. On the other hand, the temporal resolution of a sequence is limited by hardware constrains and the sound wave's travel time.

Some medical US devices also feature "elastography" capabilities. Elastography refers to the assessment of the mechanical properties of human tissue, such as its elastic moduli and viscosity (Sarvazyan et al., 2011). In particular, ultrasound elastograhy (USE) is a promising technique due to the availability and cost-efficiency of US devices (Gennisson, Deffieux, Fink, & Tanter, 2013). USE has demonstrated potential for early diagnose of pathologies, such as cirrhotic liver disease (Mueller, 2020) and breast cancer (Doyley, Meaney, & Bamber, 2000).

All USE methods share a similar structure (Sarvazyan et al., 2011). First, tissue is mechanically excited using manual pressure (Ophir, Céspedes, Ponnekanti, Yazdi, & Li, 1991), acoustic radiation force (Rudenko, Sarvazyan, & Emelianov, 1996), an external vibrator (Sandrin, Tanter, Gennisson, Catheline, & Fink, 2002) or even endogenous movements of the body such as heartbeats (Kanai, 2005; Fujikura et al., 2007). Second, the tissue's displacement response is tracked using ultrasound (Gennisson et al., 2013), hydrophones (Fatemi & Greenleaf, 1999) or superficial pressure sensors (Sarvazyan, Rudenko, Swanson, Fowlkes, & Emelianov, 1998). Finally, a physical model is used to infer the tissue's mechanical properties from the displacement information.

The second step, namely displacement estimation, plays a critical role in the performance of USE methods (Viola & Walker, 2003). Displacement estimation algorithms receive a collection of radio frequency (RF) images as input, i.e. 2D frames taken at different times: $r(x, z, T)$. The RF data is obtained from the echoes of scatterers that may be moving between frames. The algorithm's output is that displacement field $\vec{u}(x, y, z, T)$, which is a function of space and time. Some difficulties may arise when the data is corrupted by electronic and decorrelation noise (Walker & Trahey, 1995) and the magnitude of the displacement is smaller than an axial sample length, i.e. a "sub-sample" displacement (G. Pinton, Dahl, & Trahey, 2006).

In this work, a new method for estimating displacements using a bayesian approach is presented. Many displacement estimators have been proposed over the last three decades, but their performance has commonly been limited by the Crámer-Rao lower bound (CRLB) (Walker & Trahey, 1995). Nonetheless, bayesian estimators have recently been able to surpass that limit (Byram, Trahey, & Palmeri, 2013a; Byram, Trahey, & Palmeri, 2013b; Dumont & Byram, 2016). They consist of two components: a likelihood function and a prior. Previously, the normalized cross-correlation (NCC) or the sum of squared differences (SSD) have been implemented as likelihood functions. However, they are limited to offline processing, because they require oversampling or interpolation to determine sub-sample displacements. This paper introduces a novel likelihood function, called "autocorrelation kernel" (ACK), which is based on the autocorrelator algorithm proposed by Loupas, Powers, and Gill (1995) and can be directly evaluated at sub-sample lags. Thus, it is a promising technique for real-time processing.

Its target application is shear wave elasticity imaging (SWEI), a USE technique that uses ultrasound to both mechanically excite the tissue and then track the induced displacement (Sarvazyan et al., 1998). In SWEI, the transducer is electrically excited with a specially lengthy voltage sequence, called the “push” sequence, resulting in a powerful sound burst. This burst excerpts a spatially focused force in the positive axial direction called acoustic radiation force (ARF). Consequently, shear waves propagate away from the focus in the lateral direction and displace particles in the axial direction. Their propagation speed is related to the tissue’s mechanical properties, thus it is tracked using pulse-echo US. However, their magnitude is generally smaller than a sample length (in the order of tens of μm) (M. Palmeri & Nightingale, 2004).

The algorithms were tested using the simulation procedure shown in figure 1.4. First, the pushing force $f(x, y, z, T)$ was simulated. Then, the finite element method (FEM) was used to approximate the tissue’s response $\vec{u}(x, y, z, T)$ under various material conditions. Next, the imaging region was randomly populated with scatterers and B-mode images $r(x, z, T)$ were generated. The displacement $\vec{u}(x, y, z, T)$ was used to move the scatterers between each simulated acquisition. Then, an estimation of the axial component of the displacement $\hat{u}(x, z, T)$ is obtained using both the proposed method and a previously validated bayesian approach (Dumont & Byram, 2016). Finally, error metrics are calculated by comparing the estimation with the true displacement.

This work is organized as follows. In section 2, a mathematical framework is presented and each simulation block is described in order. Next, section 3 presents the output of each block and analyses those results. Finally, conclusions are drawn on section 4 and future improvements are offered.

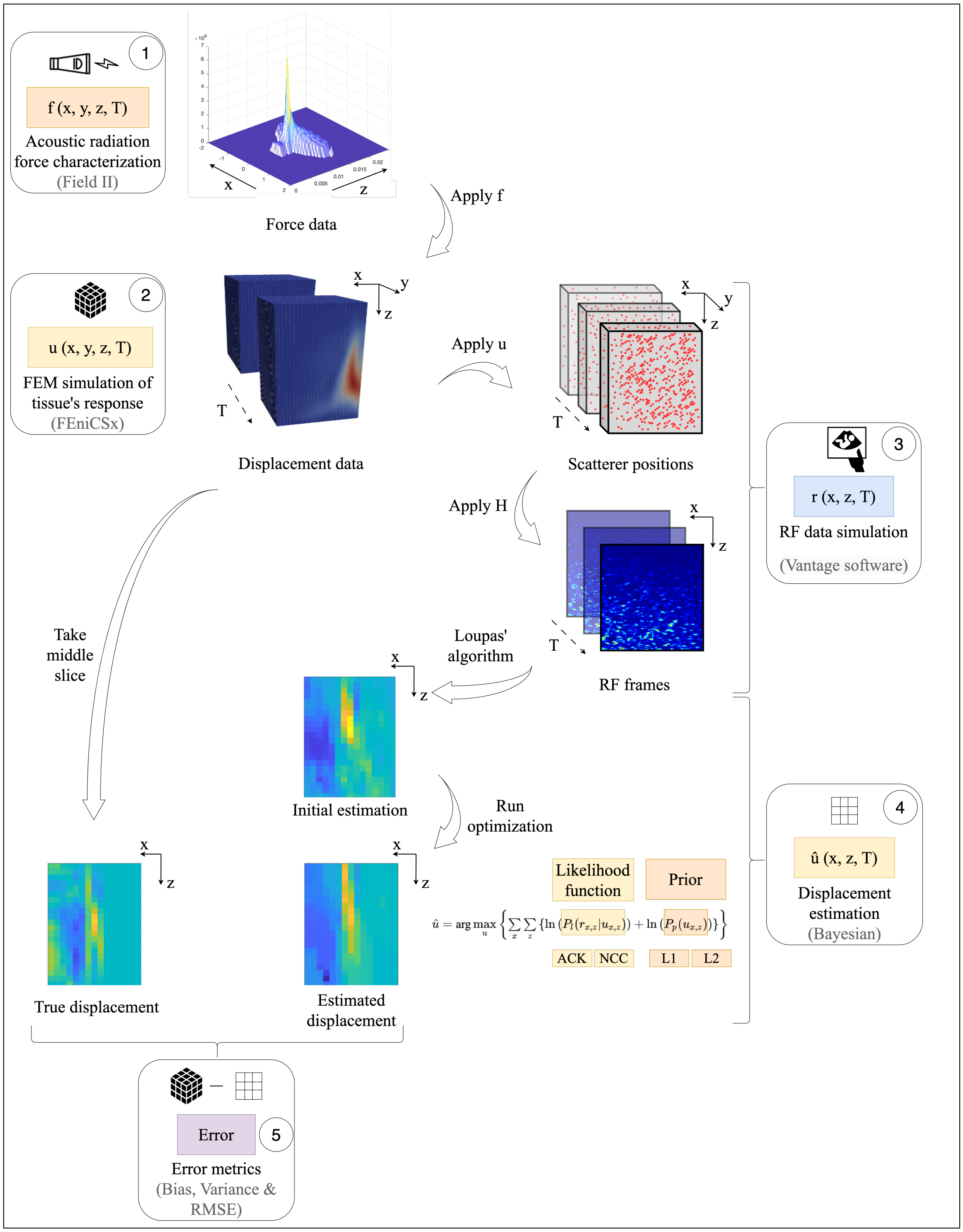

Figure 1.4. Graphical abstract of simulation procedure.

2. METHODS

2.1. Mathematical framework for images of moving tissue

As stated before, all elastography methods deal with some sort of displacement inside the tissue. This displacement can be modeled by shifting the position of a group of randomly placed scatterers (Loupas et al., 1995). For the sake of simplicity, a one-dimensional model is derived. First, a pulse-echo acquisition $r(t, T)$ is obtained at frame T. The transducer fires a pulse and then samples the echoes at times t. The sampling frequency is considerably larger than the frame rate: in the order of 10^7 versus 10^3, respectively. Therefore, dimensions t and T are also denoted as "fast" and "slow" time dimensions.

The echoes are produced by a collection of scatterers distributed along the axial direction z. The i-th scatterer is represented by a Dirac delta function $\delta(z)$ with a random reflectivity a_i and an initial axial position z_i. Position z_i can be mapped to echo arrival time t_i by using equation 1.1. If the analyzed scatterers are sufficiently close, one can assume that they are subjected to the same adimensional displacement $u(T)$, expressed as a multiple of the wavelength λ. So, a collection of N_{scat} moving scatterers can be represented by either:

$$\Delta(z, T) = \sum_{i=1}^{N_{\text{scat}}} a_i \, \delta(z - z_i - u(T) \, \lambda) \tag{2.1}$$

$$\Delta(t, T) = \sum_{i=1}^{N_{\text{scat}}} a_i \, \delta(t - t_i - 2 \, u(T) \, \lambda \, / \, c_s) \tag{2.2}$$

The collection of consecutive 1D signals received by the transducer $r(t, T)$ is obtained by taking the convolution between $\Delta(t, T)$ and $H(t)$, namely the impulse response of the acquisition setup. An example of this procedure is depicted in figure 2.1. $H(t)$ accounts for the impulse responses of the transducer, the emitted pulse and the media:

$$r(t,T) = H(t) * \Delta(t,T) \tag{2.3}$$

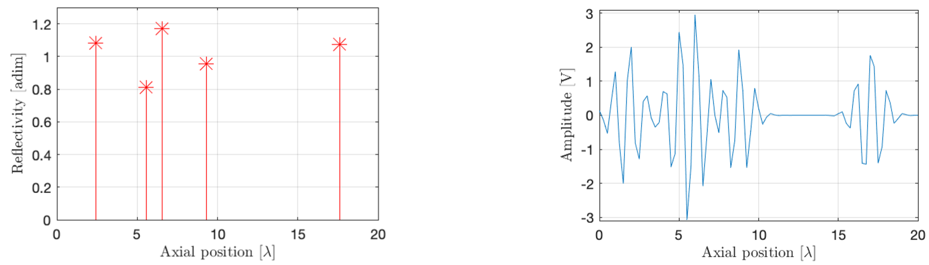

(a) Scatterer distribution $\Delta(z,T)$.

(b) Acquired signal $r(z,T)$.

Figure 2.1. Scatterer distribution and acquired signal, obtained by convolution with $H(z)$.

As shown in figures 2.2a and 2.2c, $r(t,T)$ consists on M samples in fast time t and N frames in slow time T. Inter-frame displacement is assumed to be approximately constant during the N frames. Nevertheless, the current imaging setup does not guarantee that displacements are similar during 3 or more frames, so N is set to 2 frames throughout this work, unless specified otherwise.

2.2. Non-bayesian displacement estimation algorithms

2.2.1. Normalized cross correlation function

Displacement estimation algorithms infer $u(T)$ from a set of frames $r(t,T)$, $r(t,T+1)$, etc. The most popular method for high accuracy applications consists on finding the maximum of the normalized cross-correlation (NCC) function (Svilainis, 2019). The NCC function between frames T and $T+1$ is defined as:

$$\mathrm{NCC}(\tau) = \frac{1}{\sqrt{E_r(T)E_r(T+1)}} \sum_{t=1}^{M\text{-}\tau} r(t,T)\, r(t+\tau, T+1) \tag{2.4}$$

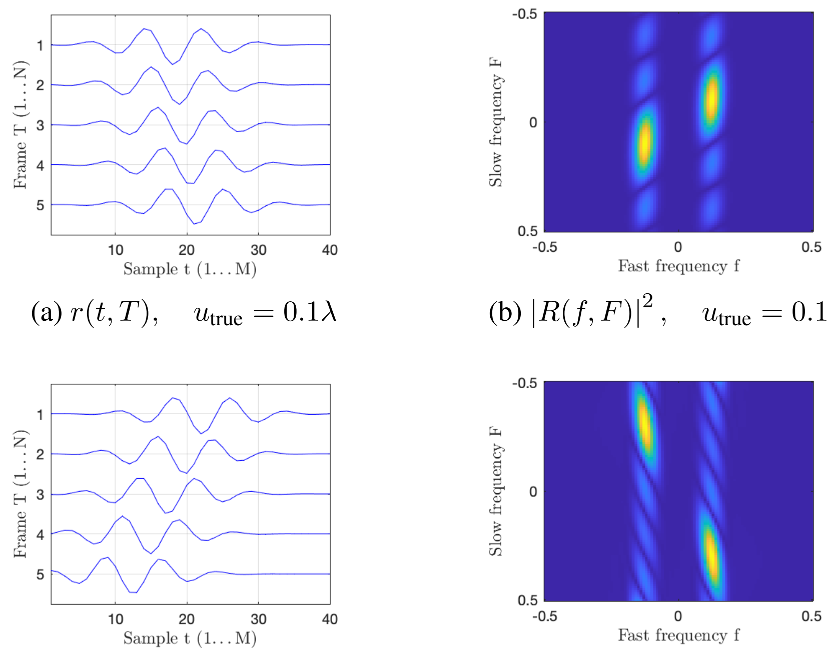

(a) $r(t,T), \quad u_{\text{true}} = 0.1\lambda$

(b) $|R(f,F)|^2, \quad u_{\text{true}} = 0.1\lambda$

(c) $r(t,T), \quad u_{\text{true}} = \text{-}0.3\lambda$

(d) $|R(f,F)|^2, \quad u_{\text{true}} = \text{-}0.3\lambda$

Figure 2.2. (a, c) One-dimensional acquisition $r(t,T)$ and (b, d) its energy spectrum $|R(f,F)|^2$. True displacement is either (upper row) $u_{\text{true}} = 0.1\lambda$ or (lower row) $u_{\text{true}} = \text{-}0.3\lambda$.

where $E_r(T) = \sum_{t=1}^{M} r^2(t,T)$ is the signal energy, τ takes integer values between 1 - M and M - 1 and $r(t,T)$ is zero for all $t \notin [1,M]$.

However, as stated in the introduction, SWEI deals with sub-sample displacements. Therefore, the NCC needs to be interpolated or oversampled to avoid quantization error. Previous works have reported good performance for small displacements using spline interpolation (G. F. Pinton & Trahey, 2006).

2.2.2. Loupas' algorithm

Alternatively, Loupas' algorithm is capable of estimating sub-sample displacements without the need of oversampling or interpolation. This is done by obtaining estimates of both the center frequency of the received signal $\hat{f}$ and its shift between various frames, i.e. the Doppler frequency $\hat{F}$ (Loupas et al., 1995). In ultrasound applications, the center frequency of the signal is in the order of MHz and belongs to the "fast" frequency dimension f, i.e. the Fourier dimension of the time between samples t. Similarly, the Doppler frequency is in the order of kHz and exists in the "slow" frequency dimension F, related to the time between frames T. Loupas et al. (1995) demonstrated that the inter-frame displacement is proportional to the ratio of their estimates $\hat{F}/\hat{f}$, which takes continuous values.

To visualize this, take the discrete time Fourier transform (DTFT) of one-dimensional frame collections $r(t, T)$ and observe the continuous energy spectral density $|R(f, F)|^2 = |\text{DTFT}\left\{r(t, T)\right\}|^2$, as in figures 2.2b and 2.2d. Notice how their spectral energy concentrates differently depending on the underlying inter-frame displacement. As a matter of fact, Loupas et al. (1995) proved that if u^* is the true displacement, then the energy spectral density of $r(t, T)$ concentrates along the line given by $F = k_{u^*}\, f$, where the slope k_{u^*} is given by:

$$k_{u^*} = \frac{u^*}{f_c\, t_s} \tag{2.5}$$

where u^* is an adimensional multiple of the wavelength, f_c is the transducer's center frequency and t_s is the fast time sampling period. Due to the fact that this line passes through the origin, the sub-sample, inter-frame displacement can be estimated by finding the centroid of the half-spectrum $(\langle f \rangle, \langle F \rangle)$ and deriving u from the slope k_u:

$$\hat{u} = \frac{\langle F \rangle}{\langle f \rangle}\, f_c\, t_s \tag{2.6}$$

The centroids are obtained as following:

$$\langle f\rangle = \frac{\int_{-0.5}^{0.5}\int_{0}^{0.5} f\ |R(f,F)|^2\ df\,dF}{\int_{-0.5}^{0.5}\int_{0}^{0.5} |R(f,F)|^2\ df\,dF}, \qquad \langle F\rangle = \frac{\int_{-0.5}^{0.5}\int_{0}^{0.5} F\ |R(f,F)|^2\ df\,dF}{\int_{-0.5}^{0.5}\int_{0}^{0.5} |R(f,F)|^2\ df\,dF} \tag{2.7}$$

However, Loupas et al. (1995) derived a quick way of estimating these centroids by evaluating the phase of the autocorrelation function near the origin. In this manner, a fast and reliable displacement estimator for sub-sample displacements was proposed.

2.3. Tissue characterization using shear wave elasticity imaging

Before delving into the task of estimating the displacements, let's review the physical principles that give rise to the target application, SWEI. On the one hand, sound is a compressional wave and its propagation speed c_s in soft tissue is relatively constant. This is because sound speed is a function of bulk modulus B and density ρ:

$$c_s = \sqrt{B/\rho} \tag{2.8}$$

Both quantities don't vary significantly in soft tissue, because it inherits these properties from water (Martin & Ramnarine, 2010). On the other hand, "shear waves" are transverse waves and their propagation speed c_t is a function a shear modulus μ and density:

$$c_t = \sqrt{\mu/\rho} \tag{2.9}$$

Unlike bulk modulus, shear modulus depends on specific biological structures and spans a much wider range of values throughout the body (at least 7 orders of magnitude). Additionally, this type of waves travel much slower, at speeds around 1-10 m/s (Hoskins, 2010). When media is linearly elastic, homogeneous and isotropic, shear modulus μ is related to elastic modulus E by (Timoshenko & Goodier, 1969):

$$\mu = \frac{E}{2 * (1 + \nu)} \approx \frac{E}{3} \tag{2.10}$$

where the Poisson's ratio ν is set to 0.499, because tissue is assumed to be nearly incompressible.

Equation 2.9 allows SWEI to calculate the tissue's shear modulus by tracking its shear wave speed (Sarvazyan et al., 1998). Shear wave displacement $\vec{u}(x, y, z, T)$ is generated using acoustic radiation force and then captured in ultrasound acquisitions $r(x, z, T)$ by using ultrafast pulse-echo ultrasound. Next, using a displacement estimator, an approximation of its axial component $\hat{u}(x, z, T)$ is calculated. This is finally fed into a shear wave speed estimation algorithm to obtain c_t and eventually μ.

2.4. Acoustic radiation force simulation

Acoustic radiation force (ARF) is the transfer of momentum from the ultrasound wave to the medium (Rudenko et al., 1996). With conventional pulse-echo imaging, transmitted pulses are too short to produce any significant force. However, if the transducer is continuously excited during many hundreds of cycles (with a so called "push" sequence), the resultant force is then capable of producing observable displacement in the axial direction, in the order of 1-10 μm (M. Palmeri & Nightingale, 2004). Even more, if the element signals are delayed so that the push is focused, an impulsive excitation is created in the media. This kind of excitation gives rise to shear waves that displace particles in the axial direction, but travel in the lateral direction.

In this work, the ARF induced by a push sequence was simulated on Field II (Jensen & Svendsen, 1992; Jensen, 1996), an ultrasound field simulator software, following the guidelines by M. L. Palmeri, Qiang, Chen, and Urban (2017). Details are included in appendix A. Simulation properties of the linear array transducer, push sequence and media are listed in tables 2.1, 2.2 and 2.3, respectively. Linear array transducers have been commonly used in SWEI (Nordenfur, 2013; Y. Wang, 2017) and the current parameters are suited for a future implementation on a Verasonics Vantage 128 System (Verasonics, Inc., Kirkland, WA, USA) with a L11-5v probe.

Table 2.1. Transducer characteristics.

Parameter	Value	Units
Transducer model	L11-5v	-
Number of elements	128	-
Center frequency	7.6	MHz
Bandwidth	76.8	%
Element spacing	0.3	mm
Element width	0.27	mm
Element height	5	mm
Elevation focus	18	mm
Aperture size	38.4	mm

Table 2.2. Push sequence parameters.

Parameter	Value	Units
Active elements	64	-
I_{SPTA} *	15	mW/cm^2
Push cycles	430	-
Push depth	10	mm
Grid resolution	0.1	mm

*Spatial-Peak, Temporal-Average Intensity.

Table 2.3. Media acoustical parameters.

Parameter	Value	Units
Speed of Sound	1540	m/s
Wavelength @ f_c	0.203	mm
Attenuation	0.3	dB/cm/MHz
Density	1000	kg/m^3

2.5. Finite element method for simulating the tissue's response

To simulate the tissue response $\vec{u}(x, y, z, t)$ to the acoustic force, a finite element method (FEM) model of the linear elastodynamics problem was solved following the guidelines by M. L. Palmeri et al. (2017). As shown in figure 2.3, the solid body Ω in front of the transducer is split into hexahedrons or "elements" and an approximate solution $\vec{U}_k$ is obtained for each node. Then, given the material properties E and ν, initial and boundary conditions and applying the ARF as an external force, the displacement is solved recursively.

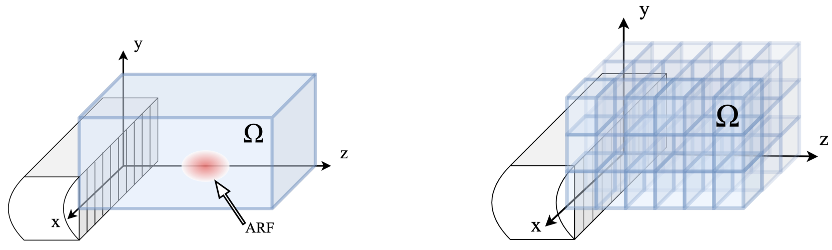

(a) FEM domain. (b) Discretized domain.

Figure 2.3. FEM domain and discretization.

The previous model was implemented using FEniCSx (Alnaes et al., 2015; Scroggs, Dokken, Richardson, & Wells, 2022; Scroggs, Baratta, Richardson, & Wells, 2022), an open-source FEM computing platform wrapped in a *python* library. Simulation parameters are described in detail in appendix B and briefly summarized here. Element size was set to 0.2 mm and material elastic modulus $E = 3\,\rho\,c_t^2$ was chosen to mimic common shear waves speed values in healthy tissue (Hoskins, Martin, & Thrush, 2010). Thus, c_t was set between 0.25 m/s and 3 m/s with steps of 0.25 m/s, resulting in E-values between 187.5 Pa and 27 kPa.

As suggested in figure 2.3a, the ARF was applied in the axial direction at the corresponding depth. To avoid reflections at boundaries, domain dimensions in the x and y directions are slightly longer than the travel distance of the respective shear wave after 2 ms. Axial size was set to 10 mm by visually inspecting a simulation on a large domain and estimating its full width in the z direction. A total of 101 time steps were simulated with a step size of $\Delta t = 20\mu$s. This temporal resolution allowed the ARF to be effectively modeled as an impulsive source, because Δt is at least 2 times smaller than the push's duration ($\approx 56\mu$s).

2.6. Simulations of B-mode acquisitions of moving tissue

To generate artificial B-mode images of the acoustically excited tissue, the Vantage software is used on "simulation mode". Specifically, virtual point scatterers are randomly placed inside an imaging region in front of the transducer. Next, they're convoluted with the spatial impulse response $H(z)$ to create a bandpass RF signal for each of the transducer's elements. These signals can be beamformed to generate a B-mode frame. A close-up to the beamformed received signals of moving scatterers can be observed in figure 2.4.

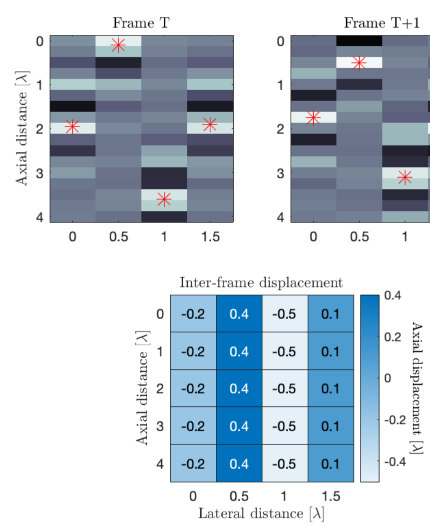

Figure 2.4. Example of 2D received signals of moving tissue. Red stars indicate the scatterers' positions. For simplicity, only one scatterer per lateral position is subjected to an axially constant displacement.

The tissue's movement is modeled by shifting the scatterers (red stars) in the axial direction between frames T and $T+1$. The shift's magnitude is obtained by linearly interpolating the displacement data from the FEM simulations in time and space. A diagram of the simulation process is depicted in figure 2.5. For each one of the 12 different material properties, 10 random scatterer placements were done. 40 frames where simulated at 20 kHz frame rate to account for the Vantage system's hardware limitations.

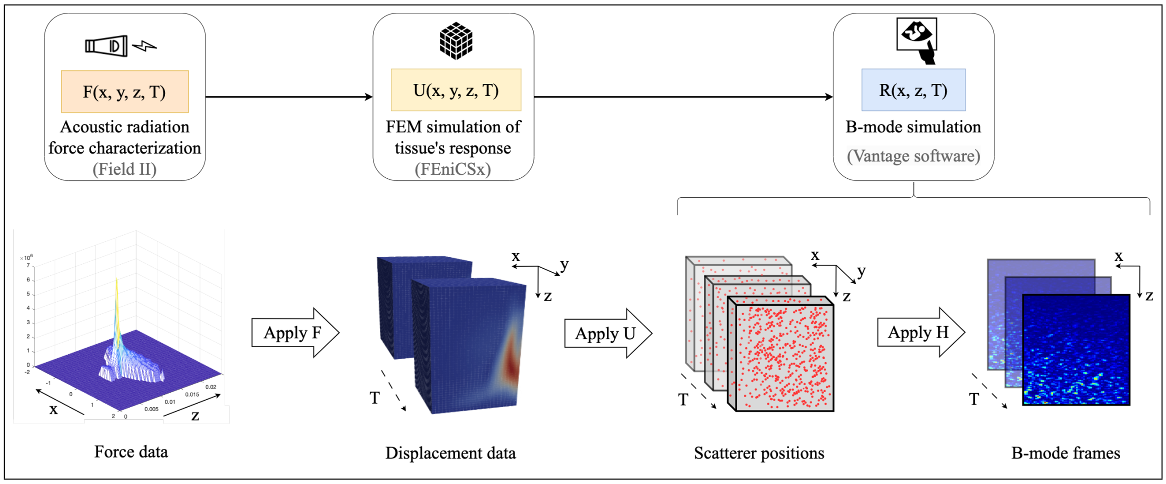

Figure 2.5. Complete diagram of simulation of b-mode images of moving tissue.

2.6.1. Imaging region of the B-mode acquisitions

The imaging region is shown in figure 2.6 and corresponds to the volume where axial displacement is significant and the transducer is sensitive. Therefore, its lateral and axial dimensions are equal to the dimensions of the largest FEM domain. Axially, the region is centered around the push's depth. Finally, its length in the elevation direction (not shown in figure 2.6) is equal to twice σ_y as described by equation 1.2.

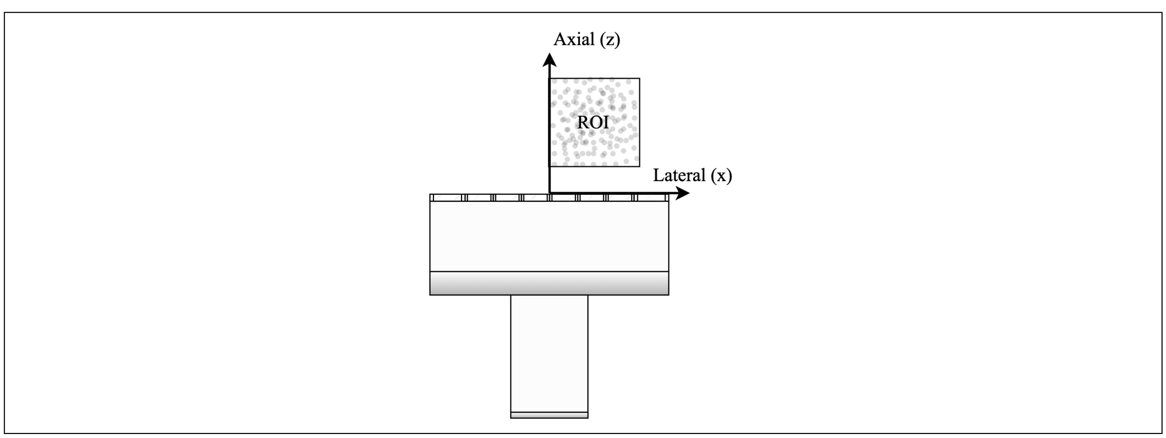

Figure 2.6. Imaging region.

As a result, the total imaged volume is 60 mm^3 and its dimensions are summarized in table 2.4. To properly imitate the texture of biological tissues (commonly called “fully developed speckle”), at least 10 scatterers should be placed per resolution cell (Wagner, Smith, Sandrik, & Lopez, 1983; Oosterveld, 1990; Yamaguchi & Hachiya, 1998). The -6 dB resolution cell was determined experimentally in Field II and found to be approx. 0.027 mm^3, thus the imaged region was populated with 22222 scatterers. Additionally, to account for noise produced by scatterers outside this region, additive Gaussian white noise with different signal-to-noise ratios (SNR) was added.

Table 2.4. Simulation region sizes.

	B-mode simulation		FEM simulation
	λ	mm	mm
Lateral (x)	30	≈ 6	0.5 - 6
Elevation (y)	5	≈ 1	0.5 - 6
Axial (z)	50	≈ 10	10

2.6.2. Plane wave imaging for ultrafast acquisitions

The imaging frame rate affects the performance of the shear wave elastography methods directly (Correia et al., 2016). An ultrafast imaging method is required to reach the hardware limit of 20 kHz and properly image the development of shear wave displacements. In SWEI, plane wave imaging (PWI) with multiple angle compounding is commonly used (Denarie et al., 2013; Nordenfur, 2013). PWI is a technique for incrementing the frame rate by transmitting a single unfocused plane wave instead of focusing the ultrasound beam at different lateral positions. Its downside is the loss of lateral resolution, which can be compensated by “steering” the plane waves at different angles and then combining them. However, to simplify the experiments and ignore the effect of artifacts related to different choices of frame rate and number of steering angles (Pan et al., 2018), single-angle PWI was preferred in this work.

2.7. Displacement estimation

Next, an estimation of the axial component of the displacement $\hat{u}(x, z, T)$ is obtained using both the proposed method and a previously validated bayesian approach (Dumont & Byram, 2016). Finally, error metrics are calculated by comparing the estimation with the true displacement.

2.7.1. Bayesian estimation

In bayesian displacement estimation, a likelihood function $P_l(r|u)$ operates over a collection of US frames $r(x, z, T)$ and assigns a value to each candidate displacement solution $u(x, z, T)$. Higher values should be assigned to candidates that are more likely to be indeed the true displacement. Non-bayesian estimators, like the NCC estimator or Loupas', usually find the u that maximizes this function. However, noise and decorrelation cause this maximum to be randomly shifted (Walker & Trahey, 1995).

Nevertheless, Bayes' theorem states that prior information can be used to update our beliefs on a certain likelihood function. So, a prior distribution $P_p(u)$ that operates solely on the candidate solution u is introduced and favors some candidates over others, for example "smooth" solutions. In turn, the objective becomes maximizing the following posterior distribution:

$$P_b(u|r) = \frac{P_l(r|u)\; P_p(u)}{\int P_l(r|u')\; P_p(u')\, du'} \tag{2.11}$$

Previous bayesian approaches have used the NCC function or the sum of squared differences as the likelihood function (Byram et al., 2013a; Byram et al., 2013b; Dumont & Byram, 2016). As stated earlier, these functions can't directly evaluate the probability of sub-sample displacements, thus some sort of oversampling or interpolation must be used. This can in turn raise the computational effort considerably and restricts its applicability to offline processing (Dumont & Byram, 2016).

2.7.2. Proposed likelihood function

A likelihood function $P_l(r|u)$ processes the received frames $r(x, z, T)$ and associates each candidate displacement u to a value. Higher values should be given to displacements that are more likely to generate the observed signals. A candidate displacement at a single location u represents an axial displacement of magnitude equal to u times the wavelength λ of the setup. In the present approach, it can take values between -0.5 and 0.5.

The proposed method turns Loupas' algorithm into a likelihood function by assigning each candidate displacement u a likelihood that is proportional to the amount of spectral energy present in the candidate's "frequency path". A frequency path is a line along the frequency dimensions f and F and its slope k_u is associated with a candidate displacement u according to the following equation:

$$F = k_u\, f, \qquad k_u = \frac{u}{f_c\, t_s} \tag{2.12}$$

Then, the likelihood of u being the true displacement is defined to be the integral along each path:

$$P_l(r|u) \triangleq \int_{-0.5}^{0.5} |R(f, k_u\, f)|^2\, df \tag{2.13}$$

If u^* is, in fact, the true displacement, then the energy integral over $F = k_{u^*}\, f$ should be greater than the integral over any other path, because energy will be concentrated around $(f, F) = (f_c, k_{u^*}\, f_c)$ (Loupas et al., 1995). Examples are presented in figure 2.7.

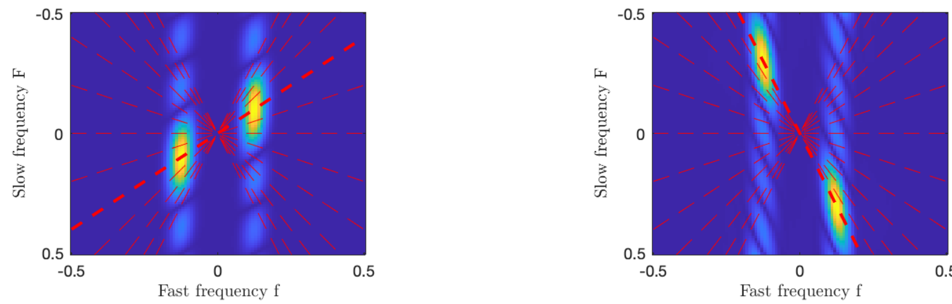

(a) $u_{\text{true}} = 0.1\lambda$ (b) $u_{\text{true}} =$ -0.3λ

Figure 2.7. Frequency paths superposed over the frequency spectrum $|R(f, F)|^2$. True displacements are (a) $u_{\text{true}} = 0.1\lambda$ and (b) $u_{\text{true}} =$ -0.3λ. Each dashed line is a candidate frequency path and the thick dashed line is the path of greater integral.

A quick calculation method is presented in appendix C. Briefly, the previous integral is equivalent to accumulating the term by term product between the autocorrelation $\gamma(t, T)$ (of size $(2M - 1) \times (2N - 1)$) and a "sinc" kernel, where $\text{sinc}\,(t) = \frac{\sin(\pi\ t)}{\pi\ t}$:

$$P_l(r|u) \propto \frac{1}{\gamma(0,0)^2} \sum_{t=1\text{-}M}^{M\text{-}1} \sum_{T=1\text{-}N}^{N\text{-}1} \gamma(t,T)\ \text{sinc}\,(t + k_u\,T) \tag{2.14}$$

2.7.3. Selectivity parameter

It's possible to apply a non-linear map to the values of the likelihood function in order to control its "confidence". Confident likelihood functions are "narrow", i.e. they assign high values to only a few candidate displacements, and diffident functions are wider. In this work, an exponential map and a selectivity parameter β are utilized for adjusting the selectivity of the distribution (Byram et al., 2013a):

$$P_l(x|u) \propto \exp\left\{\frac{1}{\beta}\frac{1}{\gamma(0,0)^2} \sum_{t=1\text{-}M}^{M\text{-}1} \sum_{T=1\text{-}N}^{N\text{-}1} \gamma(t,T)\ \text{sinc}\,(t + k_u\,T)\right\} \tag{2.15}$$

To obtain a probability density function (PDF) from a likelihood function, equation 2.16 can be used to normalize its integral to 1:

$$\mathrm{PDF}(u|r) = \begin{cases} \frac{P_l(r|u)}{\int\limits_{-0.5}^{0.5} P_l(r|u')\,du'} & \text{if } u \in [-0.5, 0.5] \\ 0 & \sim \end{cases} \tag{2.16}$$

Figure 2.8 shows the effect of β on the shape of the resulting PDF. Note that noise shifts the spectral energy away from the true displacement's frequency path, so there's an optimal value β^* that, in average, assigns more probability to the true displacement.

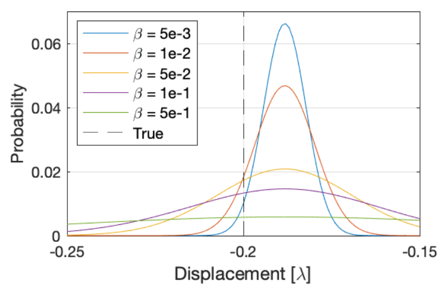

Figure 2.8. ACK's PDF at varying β. True displacement u_{true} is -0.2λ, but high noise levels (SNR = 10 dB) have shifted the distributions peak away.

2.7.4. Likelihood function benchmark

The proposed likelihood function was compared to the NCC function. Just as mentioned in section 2.2.1, the NCC function naturally assigns higher values to displacements that are more likely to be the real ones. A continuous likelihood function is formulated by interpolating the NCC at the candidate sub-sample displacement values. Again, an exponential and a parameter β are included to adjust the function's selectivity:

$$P_l(r|u) \propto \exp\left\{\frac{1}{\beta}\text{Interp}\{\text{NCC}, u\,\kappa\}\right\} \tag{2.17}$$

where κ is the number of samples per wavelength. Spline interpolation was used in the current work.

2.7.5. Prior distribution

In order to test the proposed likelihood function without altering other components of the bayesian estimator, both likelihood functions were combined with a generalized Gaussian–Markov random field prior to obtain the posterior distribution (Dumont & Byram, 2016). The non-normalized prior is given by:

$$P_p(u) \propto \exp\left\{-\frac{1}{p\,\alpha^p}\sum_{j\in\mathbb{B}}|u - u_j|_p\right\} \tag{2.18}$$

where α is the scaling parameter that controls the weight of prior information in the solution, p is the chosen vector norm and $\mathbb{B}$ is a neighbourhood of solutions. In this work, L1 and L2-norm priors were implemented. ACK likelihood was combined with both priors and NCC only with L1-norm prior. The resulting bayesian estimators will be addressed as ACK-L1, ACK-L2 and NCC-L1, respectively. To avoid problems in the calculation of gradients, the L1-norm was approximated by choosing $p = 1.05$ and calculating (Dumont & Byram, 2016):

$$|u - u_j|_1 \approx \left(\sqrt{(u - u_j)^2 + 10^{-10}}\right)^{1.05} \tag{2.19}$$

2.7.6. Posterior distribution

Finally, the displacement estimation is carried out by maximizing the posterior distribution. Notice how constant terms can be ignored without affecting the result:

$$\hat{u} = \arg\max_{u} \{P_b(u|r)\} = \arg\max_{u} \{P_l(r|u)\ P_p(u)\} \tag{2.20}$$

Furthermore, due to the monotonicity of the natural logarithm, the product of the distributions can be transformed into the sum of the log-distributions. If our goal is maximizing the sum of the posterior log-probabilities at every location of the ROI, we can split the full collection of 2D frames $r(x, z, T)$ into various windows centered at positions (x, z). For every window, a 1D frame collection $r_{x,z}(t, T)$ is obtained and its autocorrelation $\gamma_{x,z}(t, T)$ is calculated. As a result, the optimization algorithm will find the axial displacements $u_{x,z}$ so that the following expression is maximized:

$$\begin{aligned} \hat{u} &= \arg\max_{u} \left\{ \sum_{x} \sum_{z} \{\ln(P_l(r_{x,z}|u_{x,z})) + \ln(P_p(u_{x,z}))\} \right\} \\ &= \arg\max_{u} \left\{ \sum_{x} \sum_{z} \left\{ \sum_{t=1\text{-}M}^{M\text{-}1} \sum_{T=1\text{-}N}^{N\text{-}1} \frac{\gamma_{x,z}(t,T)}{\gamma_{x,z}(0,0)^2}\ \mathrm{sinc}\,(t + k_u\ T) \ldots \right.\right. \\ &\qquad \left.\left. \ldots - \frac{1}{p\ \alpha^p} \sum_{j \in \mathbb{B}} |u_{x,z} - u_j|^p \right\} \right\} \end{aligned} \tag{2.21}$$

Notice how the parameter β was removed, because parameter α is sufficient to control the relevance of both the likelihood function and the posterior distribution. This can explained by considering that multiplying the whole objective function by a constant does not alter the optimal solution. The choice of α is decided experimentally, by sweeping over a range of values and picking the one that results in the least estimation error.

The optimization was performed using the *fmincon* function provided by MATLAB (The MathWorks, Inc., Natick, MA, USA). This function uses interior-point algorithm (Byrd, Hribar, & Nocedal, 1999; Byrd, Gilbert, & Nocedal, 2000) to minimize non-linear problems. The parameters presented in table 2.5 ensure that the optimization converges to an optimum for appropriate values of α, while stopping prematurely optimizations for extremely low α values. The initial estimation was obtained using Loupas' algorithm.

Table 2.5. Non-linear optimization parameters.

	Value
Max. fun. evaluations	$2 \cdot 10^4$
Max. iterations	30
Optimality tolerance	$1 \cdot 10^{-4}$
Step tolerance	$1 \cdot 10^{-6}$
Constraint tolerance	$1 \cdot 10^{-6}$

2.8. Method evaluation

2.8.1. Likelihood evaluation

Before constructing a bayesian framework, the proposed likelihood function was compared to the NCC likelihood in terms of their best achievable performance. A good likelihood function should assign a high probability to the true displacement, even in the presence of noise. Because of this, the selectivity parameter β was varied and both likelihoods were compared using a quality metric (similar to the one proposed by Dumont and Byram (2016)):

$$Q = \operatorname*{med}_i \left\{ \sum_{u=u_i^*-\epsilon}^{u_i^*+\epsilon} \text{PDF}(u|r_i) \right\} \tag{2.22}$$

where r_i are 1000 artificially generated one-dimensional acquisitions subject to a random displacement $u_i^* \sim N(0, \frac{1}{9})$.

This quality metric indicates the median probability assigned to small neighbourhood around the actual displacement $u_{\text{true},i} \pm \epsilon$, where $u_{\text{true},i} = u_i^* \lambda$. In this case, ϵ was fixed to $\lambda/100$ and u was sampled at steps of $\lambda/1000$, thus ± 10 samples around the true displacement were considered. The best achievable performance of a likelihood function is then measured by its highest Q-value.

2.8.2. Evaluation of displacement estimates

The performance of the proposed estimators (ACK-L1 and ACK-L2) was compared with two other benchmark algorithms: non-bayesian Loupas and NCC-L1. To find the optimal α-parameter for each method, estimations were run on 4 frame collections chosen at random. They corresponded to shear wave speeds of $c_t \in \{1.5, 2, 2.5, 3\}$ m/s. Every frame was split into windows according to the parameters presented in table 2.7 and then the optimization was run using the parameters established in table 2.6. This resulted in a total of 1320 displacement estimates for each candidate α-value.

The estimations were compared in terms of bias, variance and root mean squared error (RMSE), defined as following:

$$\text{Bias}: \quad \mathbb{E}\{u^* \text{ - } \hat{u}\} \tag{2.23}$$

$$\text{Variance}: \quad \mathbb{V}\{u^* \text{ - } \hat{u}\} = \text{MSE - Bias}^2 \tag{2.24}$$

$$\text{MSE}: \quad \mathbb{E}\{(u^* \text{ - } \hat{u})^2\} = \text{Variance} + \text{Bias}^2 \tag{2.25}$$

$$\text{RMSE}: \quad \sqrt{\text{MSE}} \tag{2.26}$$

where u^* is the true adimensional displacement obtained using FEM and $\hat{u}$ is its estimation.

Table 2.6. Method parameters.

	Typical	Range
α @ ACK-L1	$5 \cdot 10^3$	$10^2 - 10^5$
α @ ACK-L2	7	$0.2 - 20$
α @ NCC-L1	10	$10^{-1} - 10^3$
Prior neighbors	3 (ax.) $\times$ 1 (lat.)	-

2.8.3. Convergence time

Finally, the computational efficiency of the bayesian methods using optimal α^* was analysed by determining the time needed for each algorithm to reach a RMSE smaller than 105% of its final value. Estimation on 4 different B-mode frames was performed. After every iteration of the non-linear optimization algorithm, error metrics were calculated and elapsed time was registered. This way, timelines of the error convergence were constructed to evaluate if the proposed method is indeed more suitable for a real-time implementation. Finally, time was expressed as a proportion of the longest computation time. In this manner, results are independent of the device where simulations were run.

Table 2.7. Imaging parameters.

	Typical	Range	Units
Axial window length	8	$2-15$	λ
Axial window hop	2	-	λ
Axial window number	22	-	-
Lateral window length	2	-	λ
Lateral window hop	2	-	λ
Lat. window number	15	-	-
Temporal ensemble	2	$[2, 3, 4]$	-
SNR	20	$[5, 20, 60]$	dB
Shear wave speed	2.5	$[1.5, 2, 2.5, 3]$	m/s

3. RESULTS

3.1. Acoustic intensity and radiation force profiles

The simulated acoustic intensity field and the resulting ARF are presented in figure 3.1. It can be seen that the sequence successfully concentrates its momentum transfer at a focus depth of 10 mm, because a spike is observed. Additionally, as recommended by M. L. Palmeri et al. (2017), a threshold of 10 % of the peak amplitude was used to crop the ARF region.

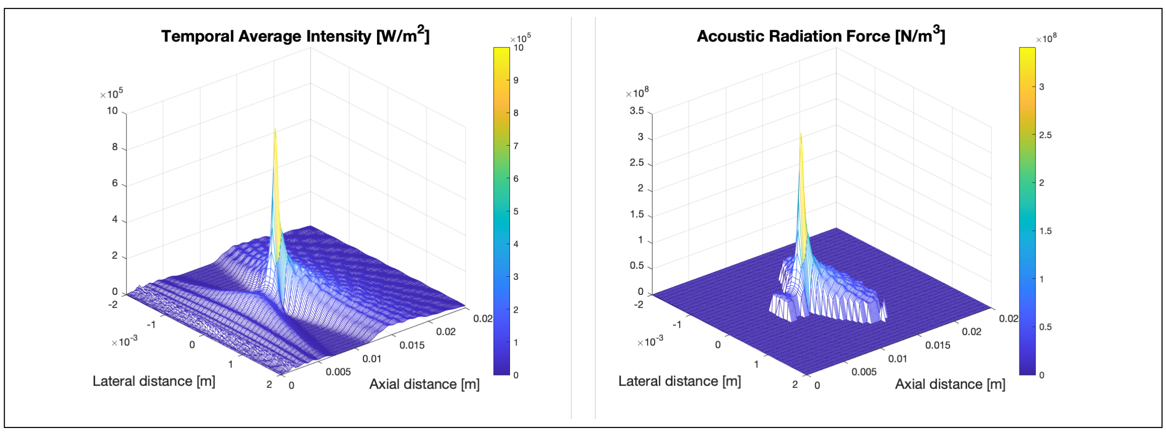

Figure 3.1. Acoustic intensity field produced by "push" sequence and resulting force density distribution.

3.2. Analysis of FEM output and tissue response

The previous ARF profile was interpolated at the nodes of the bottom X-Z facet, representing the center of the whole domain. It was applied as an external force during the push's duration and then released. The tissue displacement response was then solved using FEniCSx and visualized using the software ParaView (Kitware, Inc., Clifton Park, NY, USA). An example sequence of displacement solutions can be found in figure 3.2.

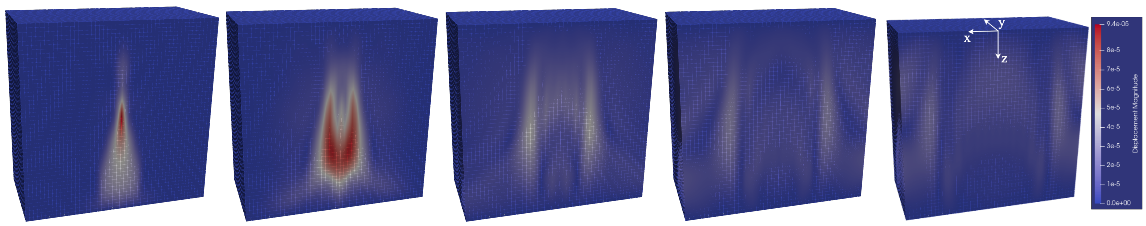

(a) $t = 0.1$ ms (b) $t = 0.5$ ms (c) $t = 1$ ms (d) $t = 1.5$ ms (e) $t = 2$ ms

Figure 3.2. Sequence of FEM solution. The domain has been reflected along the lateral direction to visualize its full lateral extension. According to the colorbar to the right, color represents the magnitude of the vector displacement. A shear wave travels laterally at a speed of $c_t = 2$ m/s.

Recall from section 2.3 that material stiffness is related to shear wave speed by $E = 3\ \rho\ c_t^2$. Results were inspected to check if shear wave speed exhibited expected values. This is done by ascertaining that the peak displacement along the lateral direction moves laterally at a speed of $c_t = \sqrt{\frac{E}{3\ \rho}}$ for a material with modulus E.

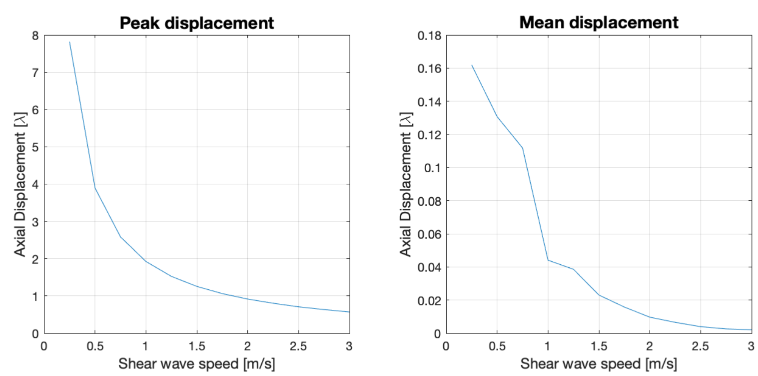

Figure 3.3. Statistics of axial displacement in FEM simulation results.

Furthermore, the peak and mean displacements were analysed for each material, as shown in figure 3.3. As it can be seen, peak displacements of softer materials are considerably larger than $\lambda/2 \approx 100\mu$m. This can be problematic, because Loupas's algorithm is restricted to inter-frame displacements of $\pm\lambda/2$. Fortunately, even in the softest material, 92.9 % of the node displacements are inside this range and only a few present larger amplitudes during initial times.

3.3. Performance analysis of the proposed method

3.3.1. Likelihood function evaluation

After processing 1000 artificially generated one-dimensional acquisitions subject to a random displacement $u_i^* \sim N(0, \frac{1}{9})$, both likelihood function were evaluated in terms of their Q-value, i.e. the median probability assigned to true displacement. This results are presented in figure 3.4. Both the proposed ACK and NCC were evaluated for different selectivity parameters β. It can be seen that results achieved with ACK are at least as good as results with NCC and even better in some cases, because their Q-values at optimal β are comparable.

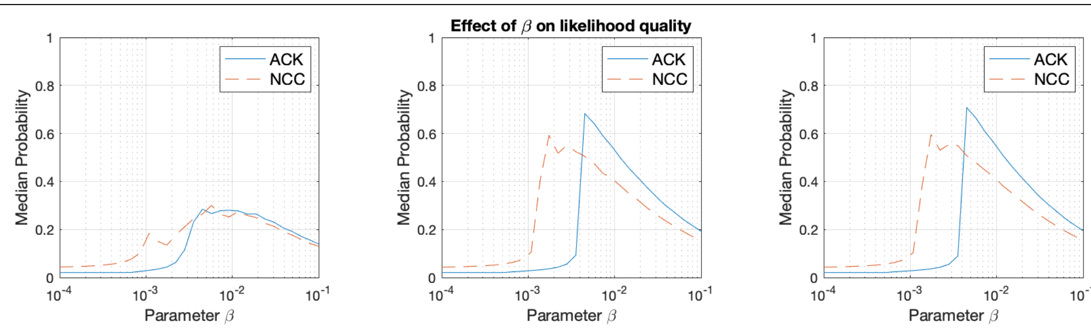

(a) SNR = 5 dB (b) SNR = 20 dB (c) SNR = 60 dB

Figure 3.4. Effect of parameter β in likelihood quality under (a) 5 dB, (b) 20 dB and (c) 60 dB SNR. ACK is compared to the NCC. $N = 2$ and axial kernel length is 8λ.

Sensibility to kernel length was also analyzed and the results are depicted in figure 3.5. Optimal β were selected based on the SNR = 20 dB simulations for both likelihood functions: $\beta^*_{\text{ACK}} = 4.6 \cdot 10^{-3}$ and $\beta^*_{\text{NCC}} = 1.8 \cdot 10^{-3}$ for ACK and NCC, respectively. Axial kernel length was varied from 2 to 15 λ. Although it was expected that longer kernels would've led to better performances, this was not the case for ACK. This can be explained by considering that longer axial lengths support the estimation of the "fast" frequency coordinate of the spectral centroid, but don't carry information about the "slow" frequency coordinate. On the contrary, more noise and no information is incorporated. In order to improve the estimation in the "slow" frequency dimension, the number of consecutive frames N has to be increased. This can be seen in figures 3.5b and 3.5c, where performance was greatly improved.

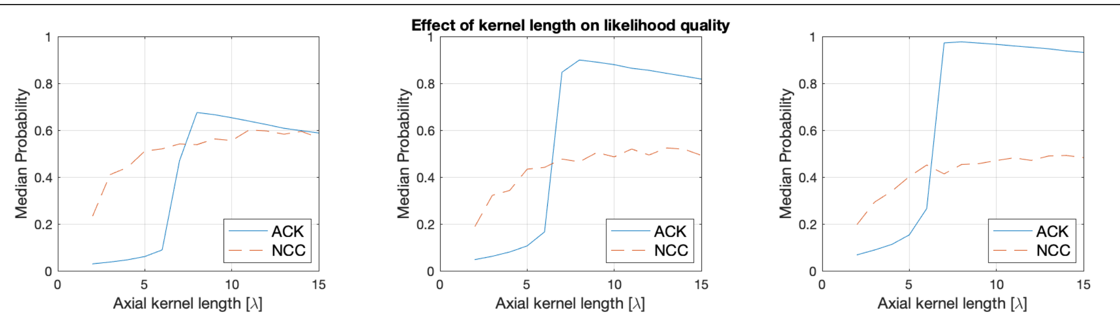

(a) $N = 2$ (b) $N = 3$ (c) $N = 4$

Figure 3.5. Effect of axial kernel length in likelihood quality for both ACK and NCC, using a number of frames N equal to (a) 2, (b) 3 and (c) 4. SNR is set to 20 dB.

3.3.2. Evaluation of displacement estimates

Displacements were estimated using ACK-L1, ACK-L2 and NCC-L1. Figure 3.6 shows an example estimation of ACK-L1 using optimal α. This corresponds to the interframe displacement between two random frames at T and $T + 1$. The spatial dimensions x and z and the displacement value u (color dimension) are expressed as adimensional multiples of the wavelength λ. Notice how there's a displacement peak near the center of the imaging region. This peak corresponds to the wavefront of the travelling shear wave. In the following frames, the lateral position of this wavefront will move towards higher values. It can be observed that the estimation with ACK-L1 is effectively smoother and less noisy than the initial Loupas estimation. This can in fact facilitate the determination of the peak's position and ultimately translate to better shear wave speed estimations.

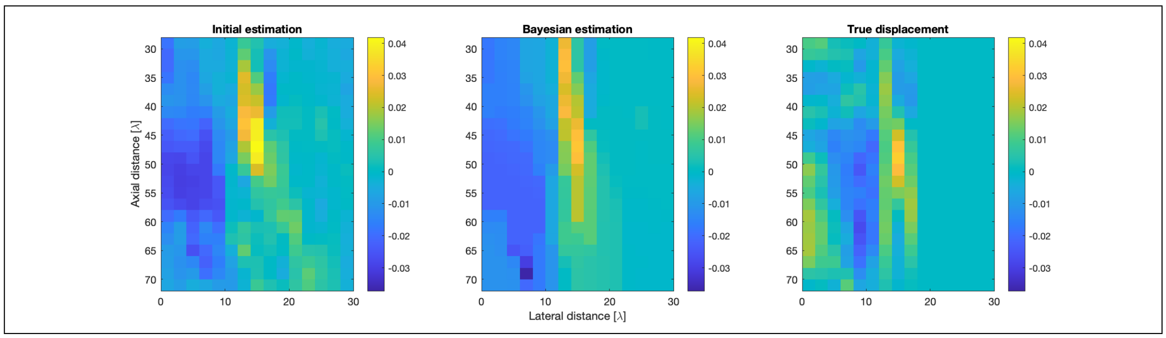

Figure 3.6. Example estimation with ACK-L1. SNR is 20 dB. Color represents the adimensional displacement value u as a multiple of λ.

The effect of α in estimation RMSE for different noise levels can be observed in figure 3.7. Notice how ACK-L1 and ACK-L2 error becomes asymptotically similar to the initial error for increasing values of α. This is expected, because large values of α cause the prior to have no effect on optimization. This ultimately leads to the maximum likelihood estimator, which is equivalent to Loupas'.

Also, note that the optimal α^* for which RMSE is minimal decreases when SNR decreases. The optimal values are summed up in table 3.1. This is expected, because higher noise levels produce noisier estimates and require a larger prior weight to intensify the spatial filtering. Another noteworthy result is that variance error is dominant (in this case, standard deviation is plotted for unit consistency). This is appropriate, because bayesian estimators trade off an increase of bias error for a reduction of variance error (Byram et al., 2013b).

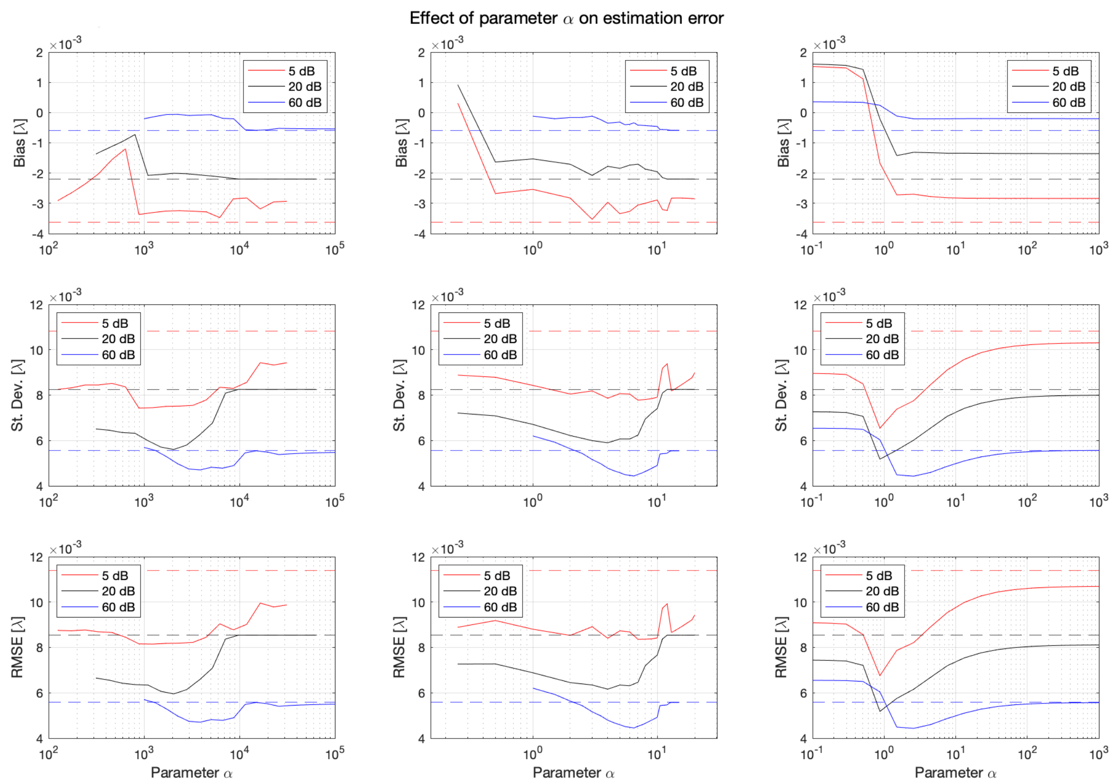

(a) ACK-L1 (b) ACK-L2 (c) NCC-L1

Figure 3.7. Effect of parameter α on estimation RMSE, using (a) ACK-L1, (b) ACK-L2 and (c) NCC-L1. Each color represents a different noise level. Continuous line corresponds to bayesian estimators and dashed line to Loupas' initial estimation. Shear wave speed is 2.5 m/s.

Table 3.1. Optimal α for different SNR.

	ACK-L1	ACK-L2	NCC-L1
5 dB	1225	2	0.9
20 dB	2050	6	0.9
60 dB	3000	7.5	1.5

Figure 3.8 helps to compare ACK-L1 and NCC-L1. Note that α-values of NCC-L1 where scaled by 10^3 to fit both curves inside the same axis. As it can be seen, performance of ACK-L1 is close to NCC-L1 for optimal values of α. Overall, ACK-L1 behaves in a expected manner with respect to its parameter α and has an optimal performance comparable to NCC-L1, so it's still a good candidate for real-time implementation if its convergence time is actually faster.

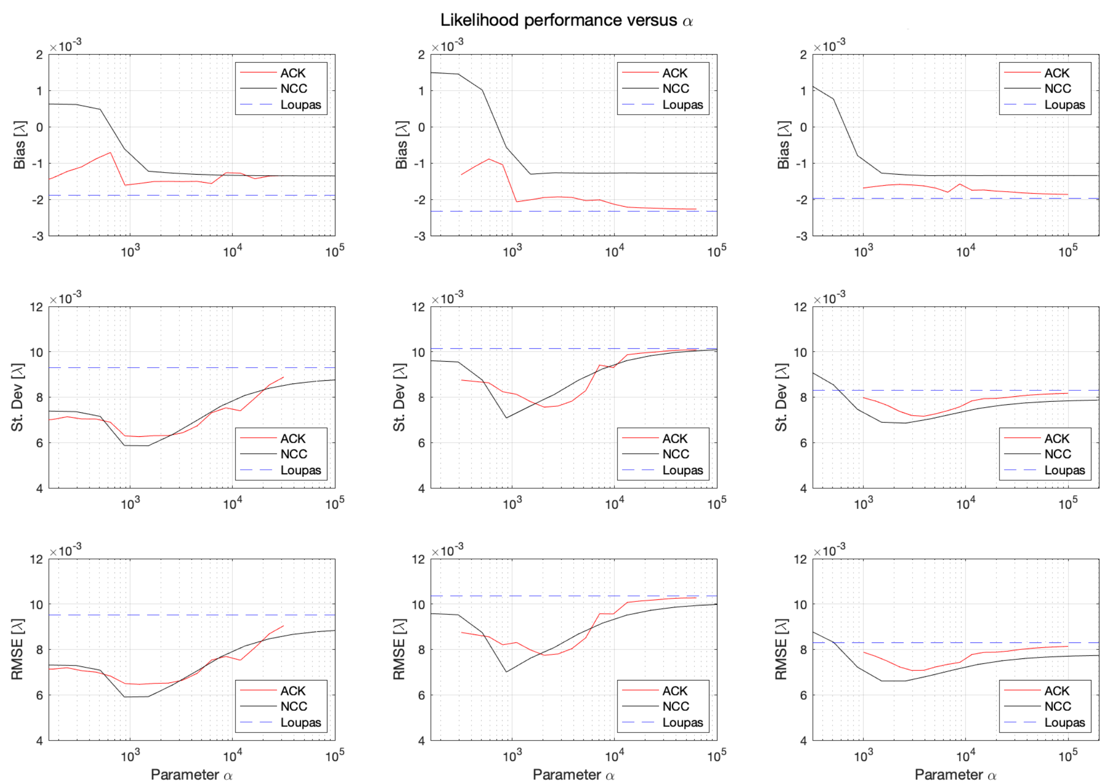

(a) SNR = 5 dB (b) SNR = 20 dB (c) SNR = 60 dB

Figure 3.8. Comparison of estimation performances versus α between ACK and NCC using a L1 norm prior. SNR is set to (a) 5, (b) 20 and (c) 60 dB. Continuous lines represent bayesian estimators and dashed line is Loupas' initial estimation. Results from shear wave speeds between 1.5 and 3 m/s were averaged.

Finally, the relative improvement to Loupas' algorithm for each bayesian estimator at optimal α is presented in table 3.2. This was calculated by dividing the decrease of RMSE by the RMSE of the initial estimation, thus providing a relative measure of RMSE improvement. Results from frames at various shear wave speeds were averaged.

Table 3.2. Relative improvement for optimal α at different SNR.

	SNR = 5 dB	SNR = 20 dB	SNR = 60 dB
ACK-L1	36.7%	21.7%	16.6%
ACK-L2	33.8%	19.3%	19.5%
NCC-L1	42.5%	27.2%	24.2%

3.3.3. Convergence time

RMSE is plotted versus time in figure 3.9 and the results of convergence time measurements are presented in table 3.3 for each method and noise scenario. As it can be seen, ACK-L1 doesn't converge faster than NCC-L1 to its final value, although each function evaluation is 28.6% faster with ACK than NCC. ACK-L1 executes in average 84.8 evaluations per second, while NCC-L1 runs only 65.9 eval./s. The fastest converge time was achieved by ACK-L2, which also has the fastest evaluation rate at 103.4 eval./s. Nonetheless, it's still necessary to combine NCC with L2-norm prior to draw conclusions.

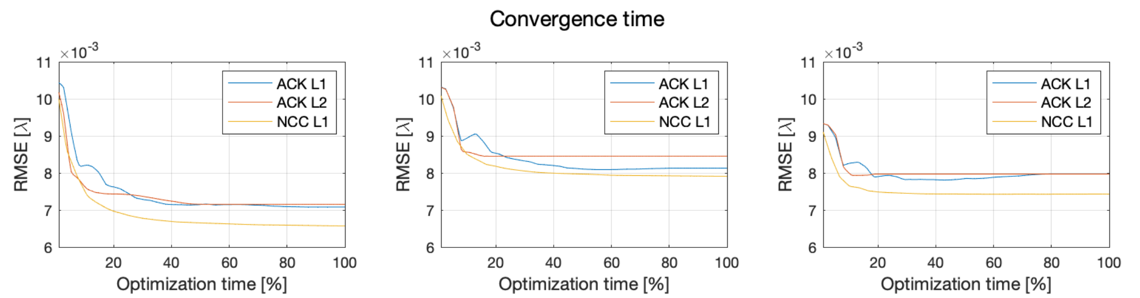

(a) SNR = 5 dB (b) SNR = 20 dB (c) SNR = 60 dB

Figure 3.9. Comparison of convergence time between ACK using a L1 and L2 norm prior and and NCC using L1 norm prior. Estimation RMSE is plotted against time. SNR is (a) 5, (b) 20 and (c) 60 dB. Results from shear wave speeds between 1.5 and 3 m/s were averaged.

Table 3.3. Convergence time for optimal α at different SNR.

	SNR = 5 dB	SNR = 20 dB	SNR = 60 dB
ACK-L1	26.7 %	20.7 %	8.0 %
ACK-L2	13.3 %	8.7 %	8.7 %
NCC-L1	24.0 %	16.0 %	8.7 %

4. CONCLUSIONS

4.1. Concluding remarks

In summary, a new likelihood function for bayesian estimation of sub-sample displacements called “autocorrelation kernel” (ACK) has been proposed. Its main objective is tracking axial displacements produced by shear waves in the context of SWEI. Unlike previously proposed likelihood functions, ACK can directly evaluate the probability of sub-sample displacements without the need of oversampling or interpolation. Thus, it is an attractive candidate for enabling real-time implementation of bayesian estimation.

ACK’s performance was compared to a non-bayesian Loupas’ estimator and a bayesian estimator with normalized cross-correlation (NCC) likelihood function. A virtual test environment was created to simulate an appropriate acoustic radiation force distribution. The simulated force was applied to a FEM model to replicate realistic shear wave displacements. The resulting displacements were applied to an ultrasound simulation software to generate B-mode images of moving tissue. Finally, displacement between frames was estimated using the proposed and benchmark methods.

Results showed that all algorithms produced a relative improvement to the initial Loupas’ estimation. However, NCC-L1 still generated better estimates than the proposed algorithms. ACK-L1 improved the initial estimation between 16.6% and 36.7%, ACK-L2 by 19.3% to 33.8% and NCC-L1 between 24.2% and 42.5%. Regarding computation time, it was found that, when using an L1-norm prior, function evaluation was in average 28.6% faster with ACK than NCC. However, this did not translate into consistently faster convergence times.

4.2. Future work

Although ACK exhibited no major performance improvement over NCC, there's still room for improvement. As stated in section 3.3.1, ACK greatly benefits from incorporating more consecutive frames into the estimation. This is a crucial difference to NCC, for which averaging results of many consecutive frame pairs does not translate into a significantly better performance. However, inter-frame displacements have to be as constant as possible throughout the whole frame collection for this method to work, which requires even faster frame rates. Fortunately, this can be done with recent frame interpolation techniques (Mirarkolaei, Snare, Schistad Solberg, & Steen, 2020; Afrakhteh, Jalilian, Iacca, & Demi, 2022) without the need of dedicated hardware.

Results also indicate that computation time is still an obstacle for real-time implementations. But, considering ACK can be evaluated for each image window independently, the algorithm can be parallelized to further decrease computation time. This parallel computing approach has already been implemented for NCC outside the context of ultrasound elastography (X. Wang & Wang, 2009; X. Wang, Wang, & Han, 2019). This might finally allow the real-time implementation of bayesian estimators.

REFERENCES

Afrakhteh, S., Jalilian, H., Iacca, G., & Demi, L. (2022). Increasing the frame rate of echocardiography images based on a novel interpolation technique. In *2022 ieee international ultrasonics symposium (ius)* (p. 1-4). doi: 10.1109/IUS54386.2022.9958853

Alnaes, M. S., Blechta, J., Hake, J., Johansson, A., Kehlet, B., Logg, A., … Wells, G. N. (2015). The FEniCS project version 1.5. *Archive of Numerical Software*, *3*. doi: 10.11588/ans.2015.100.20553

Byram, B., Trahey, G. E., & Palmeri, M. (2013a). Bayesian speckle tracking. part i: an implementable perturbation to the likelihood function for ultrasound displacement estimation. *IEEE Transactions on Ultrasonics, Ferroelectrics, and Frequency Control*, *60*(1), 132-143. doi: 10.1109/TUFFC.2013.2545

Byram, B., Trahey, G. E., & Palmeri, M. (2013b). Bayesian speckle tracking. part ii: biased ultrasound displacement estimation. *IEEE Transactions on Ultrasonics, Ferroelectrics, and Frequency Control*, *60*(1), 144-157. doi: 10.1109/TUFFC.2013.2546

Byrd, R. H., Gilbert, J. C., & Nocedal, J. (2000, Nov 01). A trust region method based on interior point techniques for nonlinear programming. *Mathematical Programming*, *89*(1), 149-185. doi: 10.1007/PL00011391

Byrd, R. H., Hribar, M. E., & Nocedal, J. (1999). An interior point algorithm for large-scale nonlinear programming. *SIAM Journal on Optimization*, *9*(4), 877-900. doi: 10.1137/S1052623497325107

Correia, M., Provost, J., Chatelin, S., Villemain, O., Tanter, M., & Pernot, M. (2016). Ultrafast harmonic coherent compound (uhcc) imaging for high frame rate echocardiography and shear-wave elastography. *IEEE Transactions on Ultrasonics, Ferroelectrics, and*

Frequency Control, *63*(3), 420-431. doi: 10.1109/TUFFC.2016.2530408

Denarie, B., Tangen, T. A., Ekroll, I. K., Rolim, N., Torp, H., Bjåstad, T., & Lovstakken, L. (2013). Coherent plane wave compounding for very high frame rate ultrasonography of rapidly moving targets. *IEEE Transactions on Medical Imaging*, *32*(7), 1265-1276. doi: 10.1109/TMI.2013.2255310

Doyley, M., Meaney, P., & Bamber, J. (2000, 07). Evaluation of an iterative reconstruction method for quantitative elasticity. *Physics in medicine and biology*, *45*, 1521-40. doi: 10.1088/0031-9155/45/6/309

Dumont, D. M., & Byram, B. C. (2016). Robust tracking of small displacements with a bayesian estimator. *IEEE Transactions on Ultrasonics, Ferroelectrics, and Frequency Control*, *63*(1), 20-34. doi: 10.1109/TUFFC.2015.2495111

Fatemi, M., & Greenleaf, J. F. (1999). Vibro-acoustography: An imaging modality based on ultrasound-stimulated acoustic emission. *Proceedings of the National Academy of Sciences*, *96*(12), 6603–6608. doi: 10.1073/pnas.96.12.6603

Fujikura, K., Luo, J., Gamarnik, V., Pernot, M., Fukumoto, R., Martin David Tilson, I., & Konofagou, E. E. (2007). A novel noninvasive technique for pulse-wave imaging and characterization of clinically-significant vascular mechanical properties in vivo. *Ultrasonic Imaging*, *29*(3), 137-154. (PMID: 18092671) doi: 10.1177/016173460702900301

Gennisson, J.-L., Deffieux, T., Fink, M., & Tanter, M. (2013). Ultrasound elastography: Principles and techniques. *Diagnostic and Interventional Imaging*, *94*(5), 487-495. (Ultrasound elastography) doi: https://doi.org/10.1016/j.diii.2013.01.022

Hoskins, P. (2010). Elastography. In P. R. Hoskins, K. Martin, & A. Thrush (Eds.), *Diagnostic ultrasound: Physics and equipment* (2nd ed., p. 196–214). Cambridge University Press. doi: 10.1017/CBO9780511750885.017

Hoskins, P., Martin, K., & Thrush, A. (Eds.). (2010). *Diagnostic ultrasound: Physics and* *equipment* (2nd ed.). Cambridge University Press. doi: 10.1017/CBO9780511750885

Jensen, J. (1996, 01). Field: A program for simulating ultrasound systems. *Medical and Biological Engineering and Computing*, *34*, 351-352.

Jensen, J., & Svendsen, N. (1992). Calculation of pressure fields from arbitrarily shaped, apodized, and excited ultrasound transducers. *IEEE Transactions on Ultrasonics, Ferroelectrics, and Frequency Control*, *39*(2), 262-267. doi: 10.1109/58.139123

Kanai, H. (2005). Propagation of spontaneously actuated pulsive vibration in human heart wall and in vivo viscoelasticity estimation. *IEEE Transactions on Ultrasonics, Ferroelectrics, and Frequency Control*, *52*(11), 1931-1942. doi: 10.1109/TUFFC.2005.1561662

Loupas, T., Powers, J., & Gill, R. (1995). An axial velocity estimator for ultrasound blood flow imaging, based on a full evaluation of the doppler equation by means of a two-dimensional autocorrelation approach. *IEEE Transactions on Ultrasonics, Ferroelectrics, and Frequency Control*, *42*(4), 672-688. doi: 10.1109/58.393110

Martin, K., & Ramnarine, K. (2010). Physics. In P. R. Hoskins, K. Martin, & A. Thrush (Eds.), *Diagnostic ultrasound: Physics and equipment* (2nd ed., p. 4–22). Cambridge University Press. doi: 10.1017/CBO9780511750885.004

Mirarkolaei, H. N., Snare, S. R., Schistad Solberg, A. H., & Steen, E. N. (2020). Frame rate up-conversion in cardiac ultrasound. *Biomedical Signal Processing and Control*, *58*, 101863. doi: https://doi.org/10.1016/j.bspc.2020.101863

Mueller, S. (2020). *Liver elastography: Clinical use and interpretation*. Springer Nature.

Nordenfur, T. (2013). *Comparison of pushing sequences for shear wave elastography* (Unpublished master's thesis). KTH, School of Technology and Health (STH).

Oosterveld, B. J. (1990). *On the quantitative analysis of ultrasound signals with applications to diffuse liver disease* (Unpublished doctoral dissertation). Radboud University.

Ophir, J., Céspedes, I., Ponnekanti, H., Yazdi, Y., & Li, X. (1991). Elastography: A quantitative method for imaging the elasticity of biological tissues. *Ultrasonic Imaging*, *13*(2), 111-134. doi: https://doi.org/10.1016/0161-7346(91)90079-W

Palmeri, M., & Nightingale, K. (2004). On the thermal effects associated with radiation force imaging of soft tissue. *IEEE Transactions on Ultrasonics, Ferroelectrics, and Frequency Control*, *51*(5), 551-565. doi: 10.1109/TUFFC.2004.1320828

Palmeri, M. L., Qiang, B., Chen, S., & Urban, M. W. (2017). Guidelines for finite-element modeling of acoustic radiation force-induced shear wave propagation in tissue-mimicking media. *IEEE Transactions on Ultrasonics, Ferroelectrics, and Frequency Control*, *64*(1), 78-92. doi: 10.1109/TUFFC.2016.2641299

Pan, Z., He, Q., Liu, Z., Shr, X., Qian, L., & Luo, J. (2018). Influence of factors on motion artifacts in strain estimation with spatial angular compounding. In *2018 ieee international ultrasonics symposium (ius)* (p. 1-4). doi: 10.1109/ULTSYM.2018.8580171

Pinton, G., Dahl, J., & Trahey, G. (2006). Rapid tracking of small displacements with ultrasound. *IEEE Transactions on Ultrasonics, Ferroelectrics, and Frequency Control*, *53*(6), 1103-1117. doi: 10.1109/TUFFC.2006.1642509

Pinton, G. F., & Trahey, G. E. (2006). Continuous delay estimation with polynomial splines. *IEEE Transactions on Ultrasonics, Ferroelectrics, and Frequency Control*, *53*(11), 2026-2035. doi: 10.1109/TUFFC.2006.143

Reddy, J. N. (2019). *Introduction to the finite element method*. McGraw-Hill Education.

Rudenko, O., Sarvazyan, A., & Emelianov, S. (1996, 05). Acoustic radiation force and streaming induced by focused nonlinear ultrasound in a dissipative medium. *Journal of The Acoustical Society of America - J ACOUST SOC AMER*, *99*. doi: 10.1121/1.414805

Sandrin, L., Tanter, M., Gennisson, J.-L., Catheline, S., & Fink, M. (2002). Shear elasticity probe for soft tissues with 1-d transient elastography. *IEEE Transactions on Ultrasonics, Ferroelectrics, and Frequency Control*, *49*(4), 436-446. doi: 10.1109/58.996561

Sarvazyan, A., Hall, T. J., Urban, M. W., Fatemi, M., Aglyamov, S. R., & Garra, B. S. (2011). An overview of elastography-an emerging branch of medical imaging. *Current medical imaging reviews*, *7*(4), 255-282. doi: 10.2174/157340511798038684

Sarvazyan, A., Rudenko, O., Swanson, S., Fowlkes, J., & Emelianov, S. (1998, 12). Shear wave elasticity imaging: A new ultrasonic technology of medical diagnostics. *Ultrasound in medicine & biology*, *24*, 1419-35. doi: 10.1016/S0301-5629(98)00110-0

Scroggs, M. W., Baratta, I. A., Richardson, C. N., & Wells, G. N. (2022). Basix: a runtime finite element basis evaluation library. *Journal of Open Source Software*, *7*(73), 3982. doi: 10.21105/joss.03982

Scroggs, M. W., Dokken, J. S., Richardson, C. N., & Wells, G. N. (2022). Construction of arbitrary order finite element degree-of-freedom maps on polygonal and polyhedral cell meshes. *ACM Transactions on Mathematical Software*. (To appear) doi: 10.1145/3524456

Svilainis, L. (2019). Review on time delay estimate subsample interpolation in frequency domain. *IEEE Transactions on Ultrasonics, Ferroelectrics, and Frequency Control*, *66*(11), 1691-1698. doi: 10.1109/TUFFC.2019.2930661

Timoshenko, S., & Goodier, J. (1969). *Theory of elasticity*. McGraw-Hill.

Viola, F., & Walker, W. (2003). A comparison of the performance of time-delay estimators in medical ultrasound. *IEEE Transactions on Ultrasonics, Ferroelectrics, and Frequency Control*, *50*(4), 392-401. doi: 10.1109/TUFFC.2003.1197962

Wagner, R., Smith, S., Sandrik, J., & Lopez, H. (1983). Statistics of speckle in ultrasound b-scans. *IEEE Transactions on Sonics and Ultrasonics*, *30*(3), 156-163. doi: 10.1109/T-SU.1983.31404

Walker, W., & Trahey, G. (1995). A fundamental limit on delay estimation using partially correlated speckle signals. *IEEE Transactions on Ultrasonics, Ferroelectrics, and Frequency Control*, *42*(2), 301-308. doi: 10.1109/58.365243

Wang, X., & Wang, X. (2009). Fpga based parallel architectures for normalized cross-correlation. In *2009 first international conference on information science and engineering* (p. 225-229). doi: 10.1109/ICISE.2009.603

Wang, X., Wang, X., & Han, L. (2019). A novel parallel architecture for template matching based on zero-mean normalized cross-correlation. *IEEE Access*, *7*, 186626-186636. doi: 10.1109/ACCESS.2019.2961334

Wang, Y. (2017). *Computational ultrasound elastography: A feasability study* (Unpublished doctoral dissertation). Michigan Technological University.

Yamaguchi, T., & Hachiya, H. (1998, may). Estimation of the scatterer distribution of the cirrhotic liver using ultrasonic image. *Japanese Journal of Applied Physics*, *37*(Part 1, No. 5B), 3093–3096. doi: 10.1143/jjap.37.3093

APPENDIX

A. ARF SIMULATION PROCEDURE

To generate a push, the elements of the transducer are focused on a specific point and then excited with a lengthy voltage signal. The resulting acoustic pressure field $p(\vec{x}, t)$ (measured in Pa) can be simulated in Field II. The power per unit area carried by this field is given by its intensity (in W^2/m), which is obtained as $I(\vec{x}, t) = p^2(\vec{x}, t)/z$, where $z = \rho\, c_s$ is the acoustic impedance of the medium (in Pa s/m^3). Once the intensity field is known, the ARF (in N/m^3) can be obtained as:

$$F(\vec{x}) = \frac{2\, \hat{a}\, \langle I(\vec{x}, t) \rangle}{c_s} \tag{A.1}$$

where $\hat{a}$ is the media absorption coefficient (in Np/m), $\langle I \rangle$ is the temporal average of the intensity and c_s is the speed of sound. $\hat{a}$ is related to the attenuation coefficient a (commonly assumed to be ≈ 0.3 dB/cm/MHz) and the transducer central frequency f_c using $\hat{a} = a\, f_c\, \ln(10)/20$.

B. FEM SIMULATION PROCEDURE

First, the domain Ω is split into hexaedral elements of size 0.2 mm. By taking advantage of symmetry in the lateral and elevational directions, it's possible to simulate only a quarter of the full domain. Then, given the material properties E and ν, conditions on the boundary $\partial\Omega$ and applied forces $\vec{f}$, the following system of equations is solved:

$$\mathbf{K}\,\vec{U}(t) + \mathbf{M}\,\ddot{\vec{U}}(t) = \vec{F}(t) \tag{B.1}$$

$$\mathbf{K}: \qquad K_{ij} = \int\limits_{\Omega} \lambda \left(\nabla \cdot \vec{\psi}_i\right) \left(\nabla \cdot \vec{\psi}_j\right) + 2\mu\, \varepsilon(\vec{\psi}_i) : \varepsilon(\vec{\psi}_j)\, d\Omega \tag{B.2}$$

$$\mathbf{M}: \qquad M_{ij} = \int\limits_{\Omega} \rho \vec{\psi}_i \cdot \vec{\psi}_j\, d\Omega \tag{B.3}$$

$$\vec{F}: \qquad F_i = \oint\limits_{\partial\Omega} \psi_i \cdot [\sigma]_{ij}\, \vec{n}\, d\partial\Omega + \int\limits_{\Omega} \vec{\psi}_i \cdot \vec{f}_i\, d\Omega \tag{B.4}$$

where $\lambda = \frac{\nu E}{(1+\nu)(1-2\nu)}$ is the first Lamé parameter, $\vec{\psi}$ are the FEM interpolation functions, $[\sigma_{ij}]$ is the stress at the boundary, $\varepsilon(\vec{\psi})$ is the deformation tensor, ∇ is the Del operator and ":" indicates tensor inner product. The strain tensor is a vector function defined as:

$$\varepsilon(\vec{u}) = \frac{1}{2}\,\left(\nabla\vec{u} + (\nabla\vec{u})^T\right) \tag{B.5}$$

The system of equations arises from the weak formulation of the conservation of linear momentum (Timoshenko & Goodier, 1969). However, a Dirichlet boundary condition of zero displacement was set on both X-Y planes and every other facet possess a Neumann boundary condition of zero stress. Therefore, the integral over the boundary of the domain can be neglected:

$$\int_\Omega \lambda \left(\nabla \cdot \vec{\psi}\right) (\nabla \cdot \vec{u}) + 2\mu\, \varepsilon(\vec{\psi}) : \varepsilon(\vec{u})\, d\Omega + \int_\Omega \rho\, \vec{\psi} \cdot \ddot{\vec{u}}\, d\Omega = \int_\Omega \vec{\psi} \cdot \vec{f}\, d\Omega \tag{B.6}$$

To achieve shear waves speeds c_t between 0.25 m/s and 3 m/s with steps of 0.25 m/s, homogeneous elastic media with elastic moduli $E = 3\ \rho\ c_t^2$ (187.5 Pa to 27 kPa) were created. Domain dimensions in the lateral and elevational directions are 0.5 mm longer than the travel distance at the corresponding shear wave speed after 2 ms. This way, no significant reflections at boundaries would occur during simulation time. Axial size was set to 10 mm by visually inspecting a simulation on a large domain and estimating the full axial width of the shear wave.

At initial time, all node displacements are zero. Then, the ARF is applied at the lower facet of the domain during the push's duration (first 3 time steps) and then vanishes. This force operates only in the positive z direction. Time stepping was carried out using a finite difference approach to recursively obtain the next displacement:

$$\left(\mathbf{K} + \frac{2}{\tau_2\, \Delta t^2}\mathbf{M}\right) \vec{U}^{s+1} = \mathbf{M} \left(\frac{2}{\tau_2\, \Delta t^2}\, \vec{U}^s + \frac{2}{\tau_2\, \Delta t}\, \dot{\vec{U}}^s + \frac{1-\tau_2}{\tau_2}\, \ddot{\vec{U}}^s\right) + \vec{F}^{s+1} \tag{B.7}$$

$$\dot{\vec{U}}^{s+1} = \frac{2\tau_1}{\tau_2\, \Delta t} \left(\vec{U}^{s+1} - \vec{U}^s\right) - \frac{2\tau_1 - \tau_2}{\tau_2}\dot{\vec{U}}^s - \frac{\tau_1 - \tau_2}{\tau_2}\Delta t\, \ddot{\vec{U}}^s \tag{B.8}$$

$$\ddot{\vec{U}}^{s+1} = \frac{1}{\tau_1\, \Delta t} \left(\dot{\vec{U}}^{s+1} - \dot{\vec{U}}^s\right) - \frac{1-\tau_1}{\tau_1}\ddot{\vec{U}}^s \tag{B.9}$$

where the time stepping parameters $\tau_1 = 0.7$ and $\tau_2 = 0.72$ result in unconditionally stable simulations (Reddy, 2019).

Calculation was performed using Docker (Docker, Inc., Palo Alto, CA, USA) on a Linux virtual machine, hosted on a 4-core, 1,1 GHz Intel Core i5, 8 GB RAM Mac OS computer (Apple, Inc., Cupertino, CA, USA). Computing time for each experiment was ~ 40 min.

C. QUICK CALCULATION OF ACK LIKELIHOOD

We start by expressing the original formulation of the likelihood function:

$$\tilde{P}_l(x|u) = \int_{-0.5}^{0.5} |R(f, k_u\, f)|^2 \; df$$

The Wiener–Khinchin theorem relates the power spectrum of the signal with its autocorrelation $\gamma(t, T)$ by using the DTFT:

$$|R(f, F)|^2 = \text{DTFT}\left\{\gamma(t, T)\right\}$$

The autocorrelation $\gamma(t, T)$ is defined as following:

$$\gamma(t, T) = \sum_{t'=1-M}^{M-1} \sum_{T'=1-N}^{N-1} r(t', T')\; r^*(t - t', T - T')$$

where the complex conjugate $r^*(t, T) = r(t, T)$ since the RF lines are real-valued.

By definition, the DTFT is obtained as following:

$$\text{DTFT}\left\{\gamma(t, T)\right\} = \sum_{t=1-M}^{M-1} \sum_{T=1-N}^{N-1} \gamma(t, T) e^{-j\; 2\pi\; (t\; f + T\; F)}$$

Integrating the power spectrum along a frequency path, we get:

$$\int_{-0.5}^{0.5} |R(f, k_u\, f)|^2 \; du = \int_{-0.5}^{0.5} \left\{ \sum_{t=1-M}^{M-1} \sum_{T=1-N}^{N-1} \gamma(t, T) e^{-j\; 2\pi\; (t\; f + T\; k_u\; f)} \right\} du$$

We can rearrange the definite integral and the finite sum, thus obtaining:

$$\int_{-0.5}^{0.5} |R(f, k_u\ f)|^2\ du = \sum_{t=1-M}^{M-1} \sum_{T=1-N}^{N-1} \gamma(t,T) \int_{-0.5}^{0.5} e^{-j\ 2\pi\ (t\ f+T\ k_u\ f)}\, du$$

Using the following substitution of the integral variable $-2\pi\ f\ =\ \omega$, the integral becomes:

$$\int_{-0.5}^{0.5} |R(f, k_u\ f)|^2\ du = \sum_{t=1-M}^{M-1} \sum_{T=1-N}^{N-1} \gamma(t,T) \int_{-\pi}^{\pi} \frac{1}{2\pi} e^{j\pi\omega\ (t+T\ k_u)}\, du$$

This is in turn the definition of the 1D sinc function:

$$\operatorname{sinc}(t + T\ k_u) = \int_{-\pi}^{\pi} \frac{1}{2\pi} e^{j\pi\omega\ (t+T\ k_u)}\, du$$

Finally, the likelihood becomes:

$$\tilde{P}_l(x|u) = \sum_{t=1-M}^{M-1} \sum_{T=1-N}^{N-1} \gamma(t,T)\ \operatorname{sinc}(t + T\ k_u)$$

To account for signals with different energy, we normalize the autocorrelation by the square of the signal's energy: $1 = \frac{1}{\gamma(0,0)^2}$.